PERGAMON

International Journal of Solids and Structures 36 (1999) 2231–2258

INTERNATIONAL JOURNAL OF
SOLIDS and
STRUCTURES

Elastoplastic finite element analysis of three-dimensional fatigue crack growth in aluminum shafts subjected to axial loading

A. de-Andrés[a], J. L. Pérez[a], M. Ortiz[b,]*

[a] *Centro Politécnico Superior, Universidad Pontificia Comillas, 28015 Madrid, Spain*
[b] *Graduate Aeronautical Laboratories, California Institute of Technology, Pasadena, CA 91125, U.S.A.*

Received 5 June 1997; in revised form 28 October 1997

Abstract

We have developed a three-dimensional cohesive element and a class of irreversible cohesive laws which enable the accurate and efficient tracking of three-dimensional fatigue crack fronts and the calculation of the attendant fatigue life curves. The cohesive element governs the separation of the crack flanks in accordance with an irreversible cohesive law, eventually leading to the formation of free surfaces, and is compatible with a conventional finite element discretization of the bulk material. The versatility and predictive ability of the method is demonstrated through the simulation of the axial fatigue tests of aluminum shafts of Thompson and Sheppard (1992a, b, c). The ability of the method to reproduce the experimentally observed progression of beachmarks and fatigue life curves is particularly noteworthy. © 1999 Elsevier Science Ltd. All rights reserved.

1. Introduction

The accurate and efficient simulation of fatigue crack growth from a pre-existing flaw is central to damage-tolerance approaches to design presently in use in the aerospace industry, to cite a salient example. Of particular interest is the prediction of the rate of growth and shape of a surface crack in components of arbitrary geometry subjected to general—possibly mixed-mode—loading histories. Inevitably, this requires advanced computational capability for the tracking of three-dimensional crack fronts. Additionally, many applications of engineering interest, specially those concerned with low-strength high-toughness materials, violate the small-scale yielding assumption of linear elastic fracture mechanics and require explicit consideration of plastic—and possibly large—deformations in the component.

---

* Corresponding author. Fax: 001 818 304 0175; e-mail: ortiz@madrid.caltech.edu

PII: S0020–7683(98)00059–6

This combination of circumstances favors the use of finite element methods for the stress analysis of the component. In this context, the tracking of ductile cracks in solids undergoing large-scale plasticity has received scant attention in the computational literature. Marusich and Ortiz (1995) have developed a method of crack tracking based on continuous and adaptive remeshing, and have successfully applied the method to the simulation of orthogonal high-speed machining. While the approach is capable of accounting for large-scale plasticity and permits the competition between ductile and brittle fracture mechanisms, its generalization to three dimensions is not straightforward, specially as regards the need for automatic remeshing. Perhaps a more fundamental difficulty concerns the formulation of fatigue crack growth laws in the presence of large-scale plasticity and arbitrary mixed-mode loading. While generalizations of Paris' law based on the J-integral have been proposed, their validity is not always born out by testing (Azodi and Bachmann, 1993).

In this paper we propose an approach to fatigue life prediction based on the use of cohesive laws. Thus, we partake of the viewpoint—pioneered by Dugdale (1960), Barrenblatt (1962), Rice (1968) and others—which regards fracture as a gradual phenomenon in which separation takes place across an extended crack 'tip', or cohesive zone, and is resisted by cohesive forces. This theory of fracture permits the incorporation into the analysis of bona fide fracture parameters such as the spall strength—the peak cohesive traction—and the fracture energy—the area under the cohesive law—of the material. An appealing feature of this approach is that it does not presuppose a particular type of constitutive response in the bulk of the material, the extent of crack growth, or the size of the plastic zone. The shape and location of successive crack fronts is also an outcome of the calculations.

Most cohesive fracture laws proposed to date are reversible and history-independent (Rose et al., 1981; Needleman, 1987; Ortiz, 1988; Beltz and Rice, 1991; Rice, 1992; Ortiz and Suresh, 1993). These laws presume that the cohesive tractions exactly retrace the loading traction–opening displacement curve upon loading. While this is rigorously correct when fracture occurs at the atomistic level, where cohesion directly arises from the atomic bonds, most macroscopic decohesion processes may be expected to entail some degree of irreversibility. This requires the formulation of irreversible cohesive laws such as proposed by Needleman (1992) and Camacho and Ortiz (1996). Unloading irreversibility, leading to the accumulation of damage, is particularly critical in simulations of fatigue crack growth such as envisioned here. Our present work extends the formulation of Camacho and Ortiz (1996) to three dimensions, Section 2. Thus, cohesive surfaces are assumed to unload to the origin and mode coupling is accounted for by the simple device of introducing an effective scalar opening displacement.

Cohesive laws have been built into finite element analyses as mixed boundary conditions (Hillerborg et al., 1976; Needleman, 1987, 1990, 1992; Xu and Needleman, 1993; Planas et al., 1994; Tvergaard and Hutchinson, 1993, 1996a, b); or have been embedded into cohesive finite elements (William, 1989; Ortiz and Suresh 1993; Xu and Needleman, 1994, 1996a, b). These elements are surface-like and are compatible with general bulk finite element discretizations of the solid, including those which account for plasticity and large deformations. Cohesive elements bridge nascent surfaces and govern their separation in accordance with a cohesive law. Camacho and Ortiz (1996) have shown that mesh-size independent results are obtained when the mesh adequately resolves the cohesive zone. In Section 3, we develop a class of three-dimensional cohesive elements consisting of two quadrilatral facets. The opening displacements are described by bilinear interpolation within the element. The element is fully compatible with—and may be used to bridge—pairs of brick elements. Selected numerical validation tests which demonstrate the accuracy and convergence of the elements are discussed in Section 4. Further validation tests may be found in de Andrés (1997).

In Section 5 we demonstrate the predictive ability of the formulation by recourse to a detailed simulation of the axial fatigue tests on aluminum shafts of Thompson and Sheppard (1992a, b, c). To the best of our knowledge, the simulation of fatigue crack growth is a novel application of cohesion elements. A full three-dimensional model of a section of the shaft is formulated within the finite element code FEAP (Taylor and Simó) using an element of Simó et al. (1993) to account for plasticity within the shaft. The proposed cohesive elements lead to accurate predictions of the progression of beachmarks observed by Thompson and Sheppard (1992a, b, c). The predicted fatigue life curves, showing the dependence of crack size on number of loading cycles, are also in close agreement with observation.

2. A class of irreversible cohesive laws

In contrast to other methods of fatigue life prediction, which have largely been predicated upon a Paris-type law of fatigue crack growth, here we endeavor to track fatigue cracks by recourse to a cohesive fracture law. In this approach, the creation of new surface is the end result of a process of gradual loss of strength with increasing separation. The cohesive law determines the work of separation, or fracture energy, required for the complete formation of a free surface. In this section, we formulate a class of inelastic cohesive laws which provide the basis for the simulations of fatigue crack growth presented in Section 5.

By way of general framework, we consider a body occupying an initial configuration $B_0 \subset R^3$. The body undergoes a motion described by a deformation mapping $\boldsymbol{\varphi}: B_0 \times [0, T] \rightarrow R^3$, where $[0, T]$ is the elapsed time interval. Let $\mathbf{F}$ be the attendant deformation gradients and $\mathbf{P}$ the first Piola–Kirchhoff stress tensor (cf e.g., Marsden and Hughes, 1983). Suppose now that the body is traversed by a cohesive surface S_0. Furthermore, orient S_0 by choosing a unit normal $\mathbf{N}$. The cohesive surface then partitions the body into two subbodies $B_0^\pm$, lying on the plus and minus sides of S_0, respectively. The power imparted to the body by body forces $\rho_0\mathbf{b}$ and boundary tractions $\mathbf{t}$ is

$$\dot{W} = \sum \int_{B_0^\pm} \rho_0 \mathbf{b} \cdot \boldsymbol{\varphi} \, \mathrm{d}V_0 + \sum \int_{\partial B_0^\pm} \mathbf{t} \cdot \boldsymbol{\varphi} \, \mathrm{d}S_0 \tag{1}$$

where the sum is over the two subbodies defined by the cohesive surface. Likewise, the kinetic energy of the body is

$$K = \sum \int_{B_0^\pm} \rho_0 |\boldsymbol{\varphi}|^2 \, \mathrm{d}V_0 \tag{2}$$

The deformation power, namely, the part of the power imparted to the solid which is not expended in raising its kinetic energy, is, therefore,

$$P^{\mathrm{D}} = \dot{W} - \dot{K} = \sum \int_{B_0^{\pm}} \rho_0 (\mathbf{b} - \boldsymbol{\varphi}) \cdot \boldsymbol{\varphi} \, \mathrm{d}V_0 + \sum \int_{\partial B_0^{\pm}} \mathbf{t} \cdot \boldsymbol{\varphi} \, \mathrm{d}S_0 \tag{3}$$

Additionally, we assume balance of linear momentum, which requires:

$$\nabla_0 \cdot \mathbf{P} = \rho_0 (\boldsymbol{\varphi} - \mathbf{b}), \quad \text{in } B_0^{\pm} \tag{4}$$

$$\mathbf{P} \cdot \mathbf{N} = \mathbf{t} \quad \text{on } \partial B_0^{\pm} \tag{5}$$

$$[\![\mathbf{P} \cdot \mathbf{N}]\!] = [\![\mathbf{t}]\!] = \mathbf{0} \quad \text{on } S_0^{\pm} \tag{6}$$

In (4), $\nabla_0 \cdot$ signifies the material divergence over B_0 and $\mathbf{N}$ is the unit normal. Inserting (4) into (3), applying the divergence theorem, and making use of (5) and (6) leads to the deformation power identity:

$$P^{\mathrm{D}} = \sum \int_{B_0^{\pm}} \mathbf{P} \cdot \dot{\mathbf{F}} \, \mathrm{d}V_0 + \int_{S_0} \mathbf{t} \cdot [\![\boldsymbol{\varphi}]\!] \, \mathrm{d}S_0 \tag{7}$$

This expression generalizes the conventional deformation power identity (e.g., Marsden and Hughes, 1983) to bodies containing cohesive surfaces.

As may be seen in (7), the presence of a cohesive surface results in the addition of a new term to the deformation power identity. The duality or work-conjugacy relations between stress and deformation measures may also be looked up from (7). As in conventional solids, the first Piola–Kirchhoff stress tensor **P** does work on the deformation gradients **F** over the bulk of the body. In addition, it follows from (7) that the tractions **t** do work on the displacement jumps

$$\boldsymbol{\delta} = [\![\boldsymbol{\varphi}]\!] \tag{8}$$

or 'opening displacements' over the cohesive surface. The preceding work-conjugacy relations set the stage for the development of a general theory of cohesion in solids. In this theory, the opening displacements $\boldsymbol{\delta}$ play the role of a deformation measure, with the tractions **t** furnishing the conjugate stress measure. It is worth noting in this regard that $\boldsymbol{\delta}$ vanishes identically when the body undergoes a rigid translation, as required of a proper deformation measure.

For simplicity, we shall assume that the behavior of cohesive surfaces is local. Consequently, for the purpose of formulating a cohesive law we may restrict our attention to a point on the cohesive surface S_0. We expect the cohesive behavior to be different for opening and sliding. In order to account for this difference, we introduce a local orthonormal basis $(\mathbf{e}_1, \mathbf{e}_2, \mathbf{e}_3)$ such that $\mathbf{e}_3$ coincides with the normal $\mathbf{N}$ to the surface S_0 and $(\mathbf{e}_1, \mathbf{e}_2)$ spans the tangent plane. Thus, in this basis δ_3 is the normal opening displacement and δ_1 and δ_2 are the sliding displacements, respectively. Correspondingly, t_3 is the normal traction across the cohesive surface and t_1 and t_2 are the shear tractions, respectively.

We shall consider cohesive laws which derive from a free energy $\phi(\boldsymbol{\delta}, \theta, \mathbf{q})$ in the form

$$\mathbf{t} = \frac{\partial \phi}{\partial \boldsymbol{\delta}}(\boldsymbol{\delta}, \theta, \mathbf{q}) \tag{9}$$

where θ is the local temperature and $\mathbf{q}$ is some suitable collection of internal variables which describe the inelastic processes attendant to decohesion. The evolution of the internal variables $\mathbf{q}$ is presumed governed by a set of kinetic relations of the general form

$$\dot{\mathbf{q}} = \mathbf{f}(\boldsymbol{\delta}, \theta, \mathbf{q}) \tag{10}$$

In the sequel we shall restrict our attention to isothermal processes and the temperature θ will be omitted throughout for simplicity. The potential structure of the cohesive law is a consequence of the first and second laws of thermodynamics (Lubliner, 1972, 1973). A key benefit of this potential structure is that it reduces the identification of the cohesive law from the three independent functions $\mathbf{t}(\boldsymbol{\delta}, \theta, \mathbf{q})$ to the single function $\phi(\boldsymbol{\delta}, \theta, \mathbf{q})$.

To further simplify the formulation of mixed-mode cohesive laws, we follow Camacho and Ortiz (1996) and introduce an effective opening displacement

$$\delta = \sqrt{\beta^2(\delta_1^2 + \delta_2^2) + \delta_3^2} \equiv \sqrt{\boldsymbol{\delta}^T \mathbf{C} \boldsymbol{\delta}} \tag{11}$$

where

$$\mathbf{C} = \begin{pmatrix} \beta^2 & 0 & 0 \\ 0 & \beta^2 & 0 \\ 0 & 0 & 1 \end{pmatrix} \tag{12}$$

The parameter β assigns different weights to the sliding and normal opening displacements. Furthermore, we shall assume that the free energy potential ϕ depends on $\boldsymbol{\delta}$ only through the effective opening displacement δ. Under these conditions, the cohesive law (9) reduces to

$$\mathbf{t} = \frac{t(\delta, \mathbf{q})}{\delta} \mathbf{C} \boldsymbol{\delta} \tag{13}$$

where

$$t = \frac{\partial \phi}{\partial \delta}(\delta, \mathbf{q}) \tag{14}$$

is a scalar effective traction. It follows from (11) and (13) that the effective traction is

$$t = \sqrt{\mathbf{t}^T \mathbf{C}^{-1} \mathbf{t}} = \sqrt{\beta^{-2}(t_1^2 + t_2^2) + t_3^2} \tag{15}$$

This relation shows that β defines the ratio between the shear and the normal critical tractions. In brittle materials, this ratio may be estimated by imposing varying degrees of lateral confinement on specimens subjected to high-strain-rate axial compression (Chen and Ravichandran, 1994, 1996).

Figure 1 depicts the type of irreversible cohesive law envisioned here. Irreversibility manifests itself upon unloading. Therefore, an appropriate choice of internal variable is the maximum attained effective opening displacement $\delta_{\max}$. Loading is then characterized by the conditions: $\delta = \delta_{\max}$ and $\dot{\delta} \geqslant 0$. Conversely, we shall say that the cohesive surface undergoes unloading when it does not undergo loading. We assume the existence of a loading envelop defining a relation between t and δ under conditions of loading, Fig. 1. A simple and convenient relation is furnished by Smith and Ferrante's universal binding law

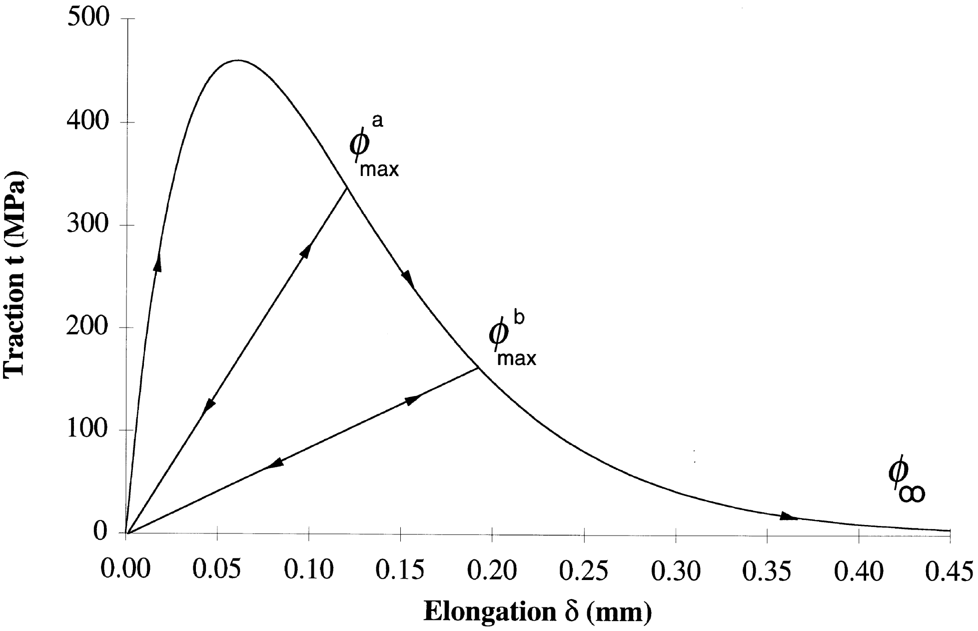

Fig. 1. Irreversible cohesive law in terms of effective traction and opening displacement, showing a Smith–Ferrante loading relation and unloading to the origin.

$$t = e\sigma_c \frac{\delta}{\delta_c} \mathrm{e}^{-\delta/\delta_c}, \quad \text{if } \delta = \delta_{\max} \quad \text{and } \dot{\delta} \geqslant 0 \tag{16}$$

where $e \approx 2.71828$ is the e-number, σ_c is the maximum cohesive normal traction and δ_c is a characteristic opening displacement. The potential corresponding to (16) is

$$\phi = e\sigma_c\delta_c \left[1 - \left(1 + \frac{\delta}{\delta_c} \right) \mathrm{e}^{-\delta/\delta_c} \right] \tag{17}$$

Following Camacho and Ortiz (1996) we shall assume unloading to the origin, Fig. 1, giving

$$t = \frac{t(\delta_{\max})}{\delta_{\max}} \delta, \quad \text{if } \delta < \delta_{\max} \text{ or } \dot{\delta} < 0 \tag{18}$$

For the present model, the kinetic relations (10) reduce to

$$\dot{\delta}_{\max} = \begin{cases} \dot{\delta}, & \text{if } \delta = \delta_{\max} \text{ and } \dot{\delta} \geqslant 0\,; \\ 0, & \text{otherwise,} \end{cases} \tag{19}$$

Evidently, the cohesive behavior just described is rate-independent. The loading cohesive law and two loading–unloading paths are shown in Fig. 1.

For nonlinear elastic materials, a standard application of the J-integral (Rice, 1968) establishes a link between the critical energy release rate G_c for crack propagation and the cohesive law. For simplicity, let the cohesive surface be flat and let $\mathbf{e}_1$ point in the direction of propagation of the crack front. Choosing a contour Γ for the evaluation of the J-integral which surrounds the cohesive zone gives

$$G_c = \int_0^R \mathbf{t} \cdot \boldsymbol{\delta}_{,1} \, \mathrm{d}x_1 = \int_0^R t\delta_{,1} \, \mathrm{d}x_1 \tag{20}$$

where R is the cohesive zone length and we have made use of (11) and (13). A change of variables enables the second of (20) to be written in the form

$$G_c = \int_0^\infty t \, \mathrm{d}\delta \equiv \phi_\infty \tag{21}$$

For the particular case of (16), (21) gives

$$G_c = e\sigma_c\delta_c \tag{22}$$

which relates σ_c and δ_c to the fracture energy G_c. In order to measure the extent of decohesion, we shall find it convenient to introduce a damage parameter

$$D = \frac{\phi(\delta_{\max})}{G_c} \tag{23}$$

Evidently, D ranges from 0–1, with these limits corresponding to an uncracked solid and a fully formed new surface, respectively. Furthermore, it follows from (19) that

$$\dot{D} \geqslant 0 \tag{24}$$

as befits the irreversibility of damage.

The precise manner in which the cohesive law accounts for fatigue crack growth deserves further comment. Envision, for definiteness, a process of cyclic loading such as depicted in Fig. 2, and consider a point on the cohesive zone at the crack tip. Suppose that the rising part of the loading curve, Fig. 2a, results in the opening of the cohesive surface. In ductile materials such as metals, this opening is inevitably accompanied by plasticity in the surrounding matrix. Consequently, upon unloading the cohesive zone does not close completely, Fig. 2b. Under these conditions, the next load rise causes the loading envelope of the cohesive law to be reached and further damage accumulates, Fig. 2c. After a sufficient number of cycles, the cohesive surface loses its integrity completely and new surface is formed, with the attendant growth of the crack.

3. Finite element implementation

A particularly appealing aspect of cohesive laws is that they fit naturally within the conventional framework of finite element analysis. One possible approach is to implement the cohesive law as a mixed boundary condition, relating tractions to displacements at boundaries and interfaces (Hillerborg et al., 1976; Needleman, 1987, 1990a, b, 1992; Xu and Needleman, 1993; Planas et al., 1994; Tvergaard and Hutchinson, 1993, 1996a, b). Here, by contradistinction, we follow William (1989) and Ortiz and Suresh (1993) and directly embed the cohesive law into surface-like finite elements, leading to the formulation of cohesive elements.

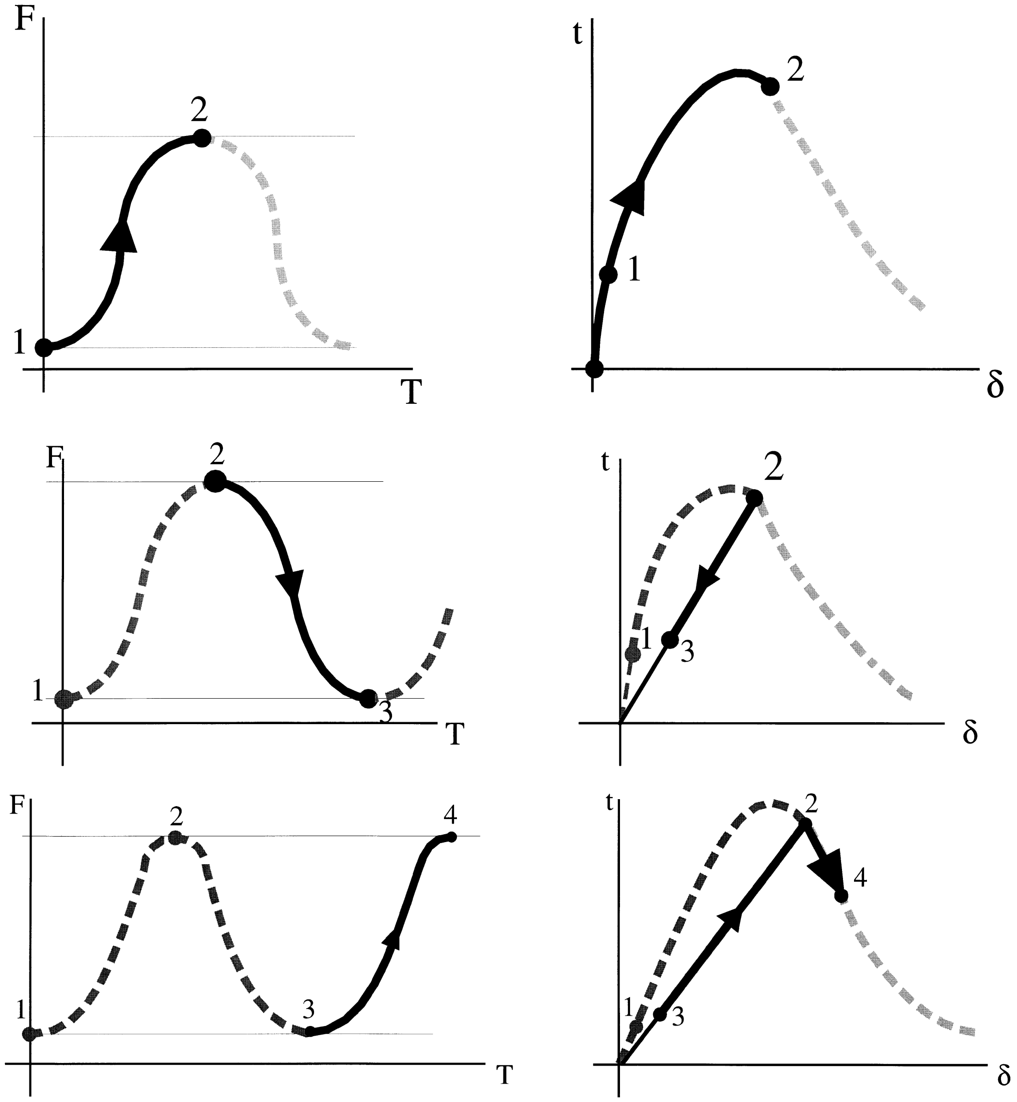

Fig. 2. Schematic representation of the process of damage accumulation during cyclic loading. (a) Opening of cohesive surface; (b) partial unloading; (c) reloading and subsequent damage.

The particular element geometry considered here is shown in Fig. 3. The element consists of two quadrilateral patches wherein the displacements are represented by bilinear interpolation. This element geometry is compatible with three dimensional brick elements. In the applications discussed in Section 5, we have used the enhanced 3-D elastoplastic brick of Simó et al. (1993). The compatibility of cohesive elements with general classes of bulk elements and constitutive behavior is again noteworthy.

As is conventional in the formulation of the displacement finite element method, we enforce equilibrium weakly by recourse to the virtual work principle:

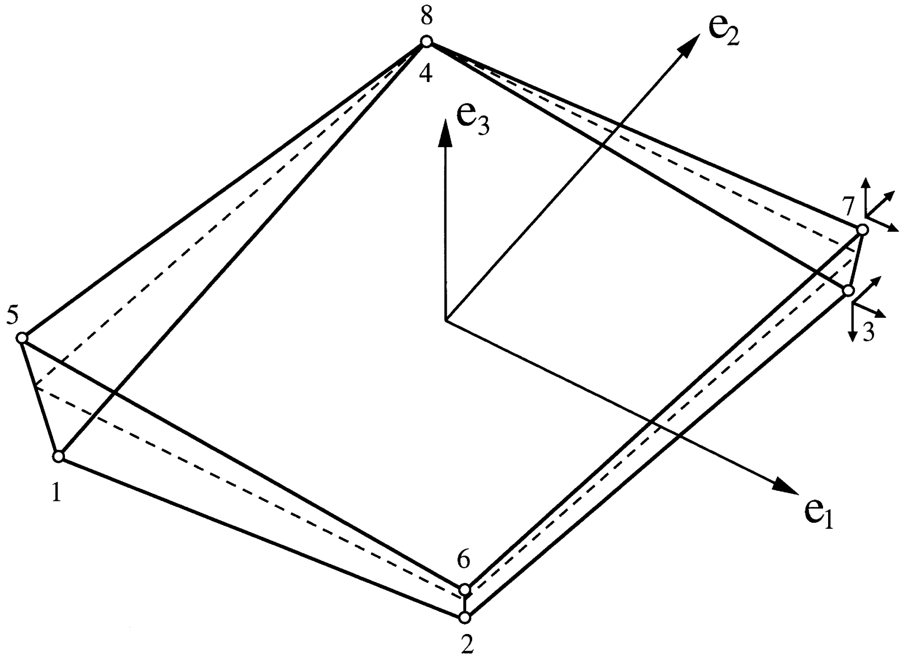

Fig. 3. Eight-node quadrilateral cohesive element compatible with brick volume elements.

$$\sum \int_{B_0^\pm} [\mathbf{P} \cdot \nabla_0 \boldsymbol{\eta} - \rho_0 \mathbf{b} \cdot \boldsymbol{\eta}] \, \mathrm{d}V_0 + \int_{S_0} \mathbf{t} \cdot [\![\boldsymbol{\eta}]\!] \, \mathrm{d}S_0 - \sum \int_{\partial B_{0,2}^\pm} \bar{\mathbf{t}} \cdot \boldsymbol{\eta} \, \mathrm{d}S_0 = 0 \tag{25}$$

where we abide by the conventions introduced in Section 2 and we have restricted attention to the quasistatic case. In addition, in (25) $\boldsymbol{\eta}$ is an arbitrary virtual displacement satisfying homogeneous boundary conditions on the displacement boundary $\partial B_{0,1}^\pm$, and $\bar{\mathbf{t}}$ are the tractions applied over the traction boundary $\partial B_{0,2}^\pm$.

For simplicity, in the remainder of this section we formulate the cohesive element within the framework of linearized kinematics. In particular, we shall not account for the rotation of the normal to the cohesive surface. This level of approximation is appropriate for most applications to fatigue crack growth, which typically involve small strain-cycle amplitudes. We adopt the local numbering convention displayed in Fig. 3 and label the nodes on the minus patch 1–4 and the nodes on the plus patch 5–8. The opening displacements across a cohesive element e are then interpolated from the corresponding nodal displacements $\mathbf{u}_a^e$ as

$$\boldsymbol{\delta}^e = \sum_{a=1}^{8} \mathbf{u}_a^e N_a^e \tag{26}$$

where N_a^e, $a = 1, \ldots, 8$ are bilinear shape functions satisfying

$$N_a = -N_{a+4}, \quad a = 1, \ldots, 4 \tag{27}$$

Substitution of the finite element interpolation into (25) leads to the usual statement of equilibrium (e.g., Simó et al., 1993) plus an additional internal force array introduced by the cohesive surface. This additional array is

$$f_{ia} = \sum_e \int_{\Sigma_0^e} t_i N_a^e \, \mathrm{d}S_0 \tag{28}$$

where Σ_0^e is the domain of cohesive element e and the sum over e extends to all cohesive elements. Likewise, the cohesive surface contributes an additional term to the tangent stiffness matrix, which follows by consistent linearization of (28). This term is

$$K_{iakb} = \frac{\partial f_{ia}}{\partial u_{kb}} = \sum_e \int_{\Sigma_0^e} S_{ik} N_a^e N_b^e \, \mathrm{d}S_0 \tag{29}$$

where

$$\mathbf{S} = \frac{\partial \mathbf{t}}{\partial \mathbf{u}} = (\phi'/\delta)\mathbf{C} + (1/2)[\phi'' - (\phi'/\delta)]\delta^{-2}(\mathbf{C}\boldsymbol{\delta}) \otimes (\mathbf{C}\boldsymbol{\delta}), \quad \text{(loading)} \tag{30}$$

$$= [\phi'(\delta_{\max})/\delta_{\max}]\mathbf{C}, \quad \text{(unloading)} \tag{31}$$

are the tangent spring constants of the cohesive surface.

Calculations proceed incrementally and are driven by a prescribed history of applied forces or displacements. For each loading step, the incremental displacements may be computed, e.g., by recourse to a Newton–Raphson iteration. However, in applications to high-cycle fatigue it would be prohibitively expensive to follow in detail every loading cycle. Instead, we seek to compute the solution at selected cycles $N_0 = 0, \ldots, N, N_{n+1}, \ldots$, with $N_{n+1} - N_n$ large. Evidently, this requires the estimation of the change in the state of the cohesive surface as quantified, e.g., by the damage variable (23), over a large number of cycles. A convenient estimate is furnished by one-term Taylor expansion:

$$D_{n+1} \approx D_n + \left.\frac{\partial D}{\partial N}\right|_n (N_{n+1} - N_n) \tag{32}$$

We compute the rate of change $(\partial D/\partial N)_n$ of D per cycle at N_n required to effect this extrapolation by a detailed step-by-step computation of a few loading cycles. The cycle increment $N_{n+1} - N_n$ used in the extrapolation formula (32) is selected so that the damage increment $D_{n+1} - D_n$ is sufficiently small. It bears emphasis that in calculations D is the only state variable which is extrapolated. Following the extrapolation of D, an equilibrium loop is entered which has the effect of updating the remaining state variables in a manner consistent with the constitutive relations.

4. Numerical test

We proceed to assess the accuracy and convergence properties of the formulation developed in the foregoing by applying it to the case of an elliptical crack in an infinite elastic solid subject remote tensile loading. Further validation tests may be found in de Andrés (1997). We consider an elliptical crack of semiaxes a and b in the ratio $k' = b/a = 0.8$. The crack opens under the action of a uniform remote normal stress σ. Points on the crack front may be parametrized by the polar angle α as $x_1 = a \cos \alpha$ and $x_2 = b \sin \alpha$. The stress intensity factors are then given by Kassir and Sih (1996)

$$K_{\mathrm{I}} = \frac{\sigma\sqrt{\pi b}}{E(k)}(\sin^2 \alpha + k'^2 \cos^2 \alpha)^{1/4} \tag{33}$$

where $k^2 = 1 - k'^2$ and

$$E(k) = \int_0^{\pi/2} \sqrt{1 - k^2 \sin^2 \phi}\, \mathrm{d}\phi \tag{34}$$

is the elliptic integral of the second kind.

The computational mesh is shown in Fig. 4. The material constants used in the calculations are roughly representative of aluminum 2024-T351 and are collected in Table 1. Owing to the symmetries of the problem the analysis may be restricted to a single octant. The computational domain is discretized into eight-node elastic brick elements and the entire plane of the crack is tiled with cohesive elements. The lateral surface of the computational domain is traction-free, and displacements are prescribed over its end sections. The radius of the computational domain is set to ten times the major semiaxis of the elliptical crack. The calculations were carried out using R. L. Taylor's finite element program FEAP (Taylor and Simó). The stress intensity factor is computed from the opening displacement δ through Irwin's energy release identity, with the result

$$K_{\mathrm{I}} = \sqrt{\frac{E\phi(\delta)}{1 - \nu^2}} \tag{35}$$

where E and ν are the Young's modulus and Poisson's ratio of the material, respectively.

The computed values of K_{I} are compared to the analytical solution for the elliptical crack in an infinite solid in Fig. 5. It should be carefully noted that the comparison is to some extent indirect owing to the finiteness of the computational domain. This caveat notwithstanding, the overall agreement between the numerical and analytical solutions is satisfactory. Figure 6 shows the percent error in the numerical solution. Again the maximum error of 3% may be considered satisfactory in view of the limited resolution of the mesh. De Andrés (1997) has applied the same

Table 1
Material constants for aluminum 2024-T351

Young's modulus (E)	72 GPa
Poisson's ratio (ν)	0.3
Yield stress (σ_Y)	311 MPa
Cohesive stress (σ_c)	460 MPa
Fracture energy (G_c)	75 MPa × mm
Ratio $\beta = \tau_c/\sigma_c$	0.5

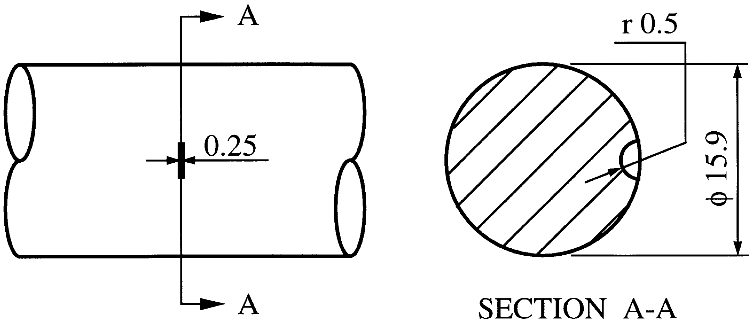

Fig. 7. Geometry of prenotched specimen (mm).

numerical approach to a Dugdale–Barrenblat semi-infinite crack in an infinite elastic solid and has established the optimal convergence of the finite element solution as the mesh size tends to zero.

5. Comparison with experiment

Thompson and Sheppard have tested prenotched aluminum 2024–T351 shafts under cyclic tension and torsion (Thompson and Sheppard, 1992a, b, c), and have reported detailed observations of the propagation of beachmark crack fronts and fatigue life curves. Their experiments thus furnish an exacting test of the predictive ability of the theory developed in the foregoing. Here we confine our attention to cyclic axial loading. Simulations concerned with torsional loading have been reported by de Andrés (1997).

The geometry of the specimen is shown in Fig. 7. The central section of the shaft has a diameter of 15.9 mm and contains a machined circular flaw of radius 0.5 mm at 90° to the axis. The applied axial loads consist of alternating tension in the range of 13.5 to 135 MPa. The material properties assumed in the calculations are collected in Table 1.

The nominal linear-elastic stress-intensity factor K at the maximum crack depth may be estimated using the formulae of Forman and Shivakumar (1986) (see also Thompson and Sheppard, 1992a). For the range of loading under consideration, K increases monotonically from an initial value of 3.5 $\text{MPa}\sqrt{\text{m}}$ to a final value of 50 $\text{MPA}\sqrt{\text{m}}$ when the crack covers nearly all the cross section of the shaft. It is interesting to note that, as expected in the fatigue of metals, the crack grows even though the stress-intensity factor remains below—in fact considerably below initially—the toughness $K_{\text{IC}} = 77$ $\text{MPa}\sqrt{\text{m}}$ of the material. A standard estimate of the corresponding plastic zone size is

$$r_p = \frac{1}{2\pi}\left(\frac{K}{\sigma_Y}\right)^2 \tag{36}$$

For the nominal range of K just noted this gives that the plastic zone size increases monotonically from an initial value of $r_p = 0.021$ mm to a final value of $r_p = 4.1$ mm. From these estimates we may expect the condition of small-scale yielding—a key requirement for the applicability of linear-elastic fracture mechanics—to be met during the early stages of growth. By contrast, when the

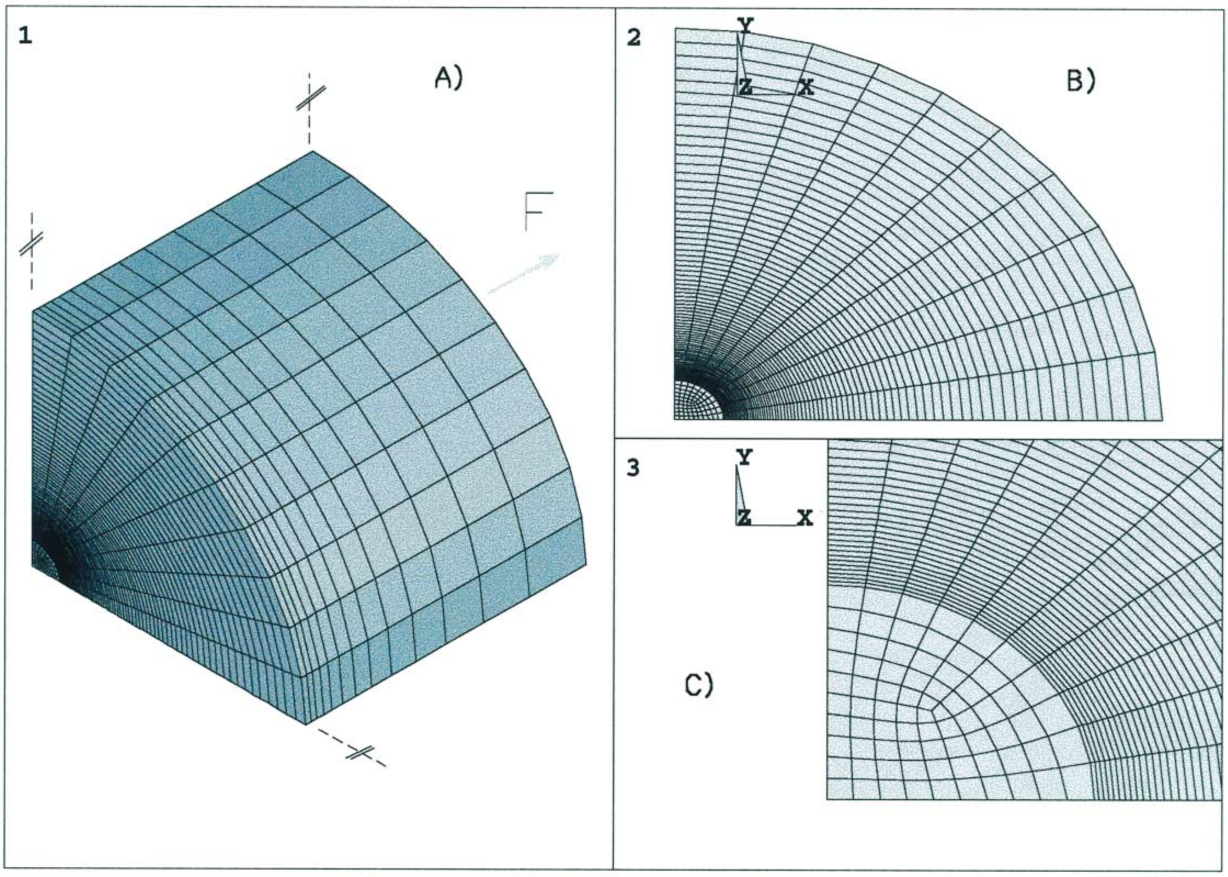

Fig. 4. Computational mesh for the analysis of an elliptical crack in an infinite elastic medium.

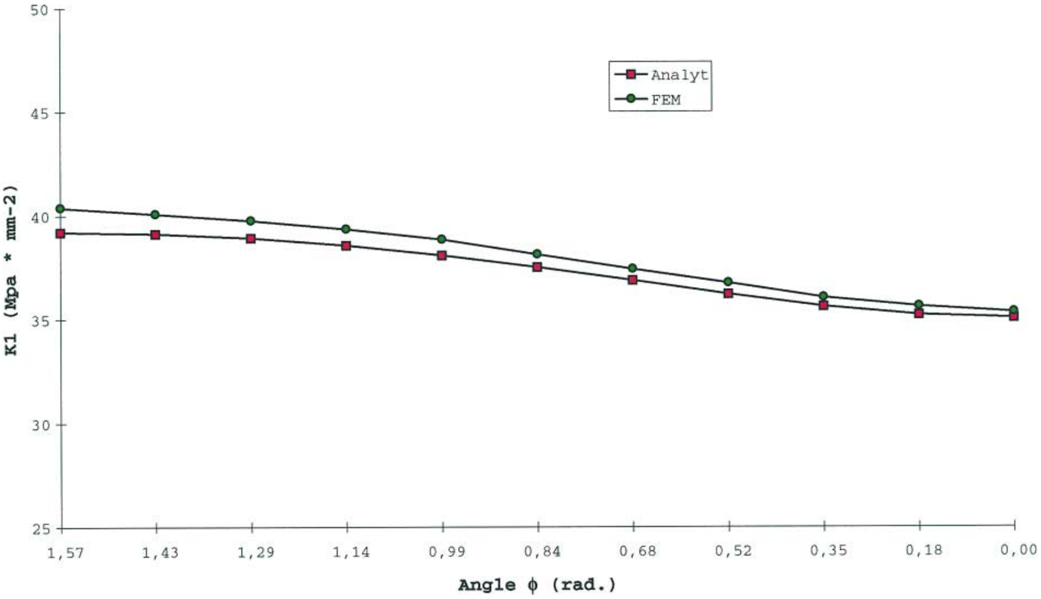

Fig. 5. Exact and computed distribution of stress intensity factor K_{IC} as a function of polar angle for elliptic crack in an infinite elastic solid.

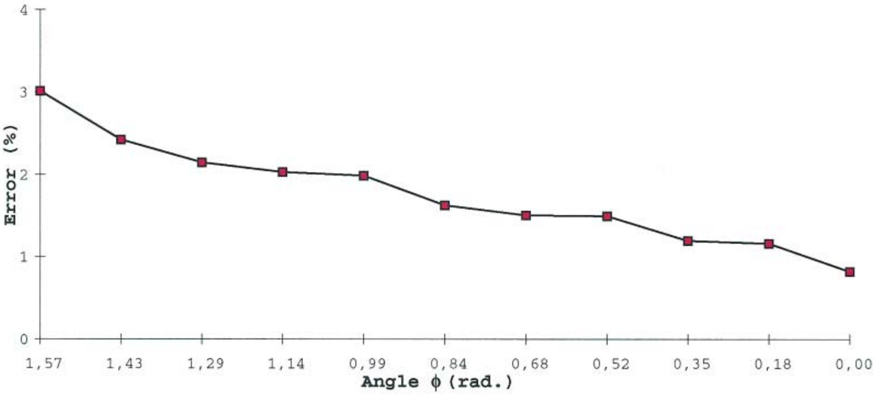

Fig. 6. Percent error in stress intensity factor K_{IC} as a function of polar angle for elliptic crack in an infinite elastic solid.

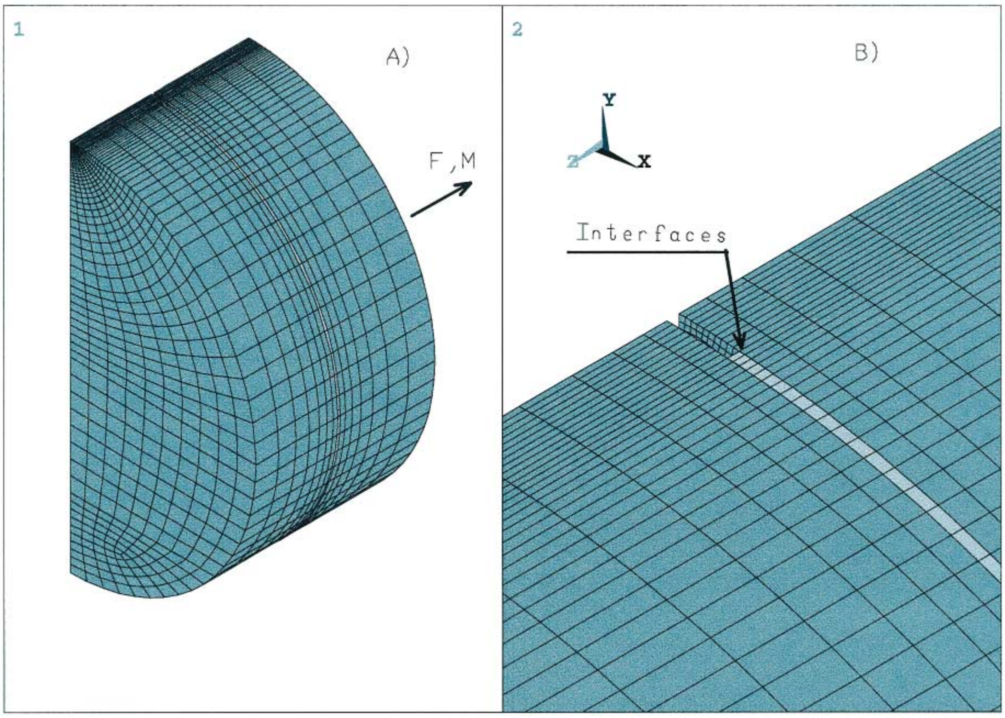

Fig. 8. Computational mesh for the analysis of aluminum shafts subjected to cyclic tensile loading, showing initial flaw and distribution of cohesive elements over the crack plane.

(a)

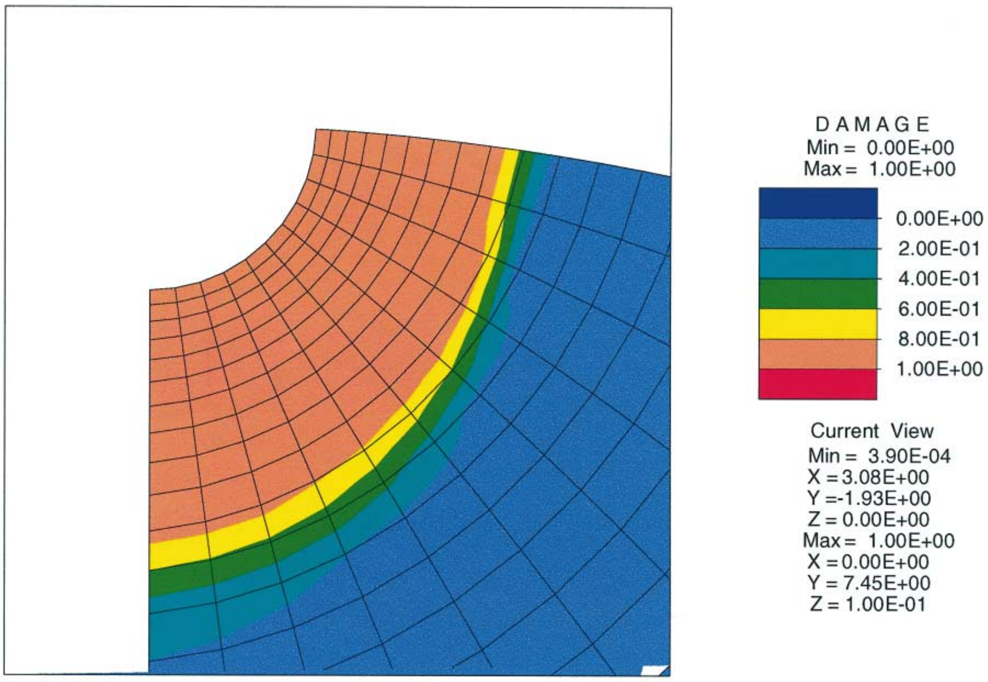

Fig. 9. Level contours of damage variable D showing the geometry of the crack ($D \approx 1$), uncracked ligament ($D \approx 0$), and cohesive zone ($0 < D < 1$). (a) $N = 255{,}000$ cycles; (b) $N = 330{,}000$ cycles; (c) $N = 340{,}000$ cycles, and (d) $N = 345{,}000$ cycles.

(b)

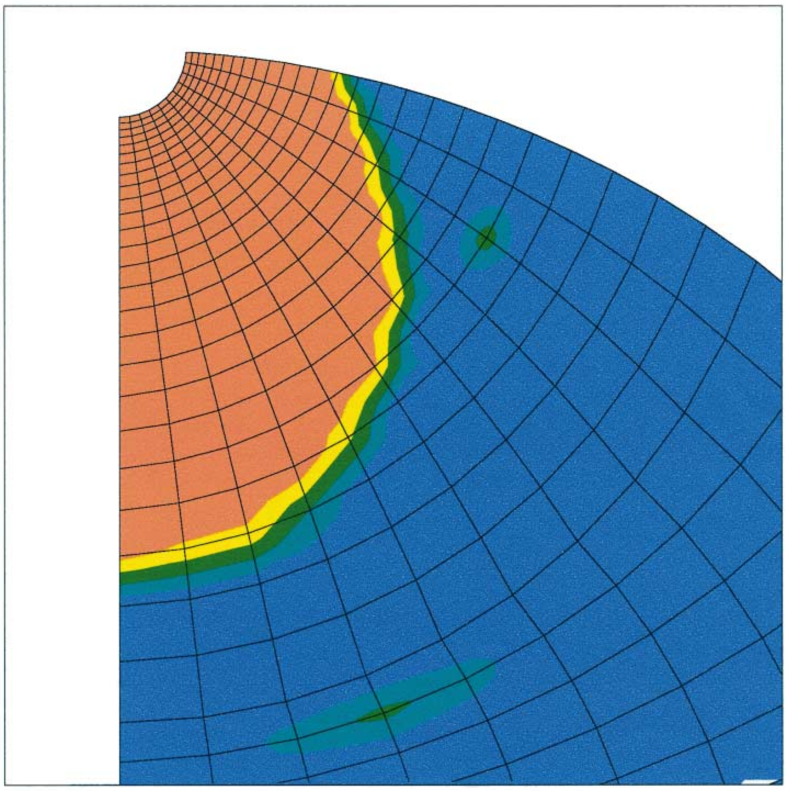

Fig. 9—continued.

(c)

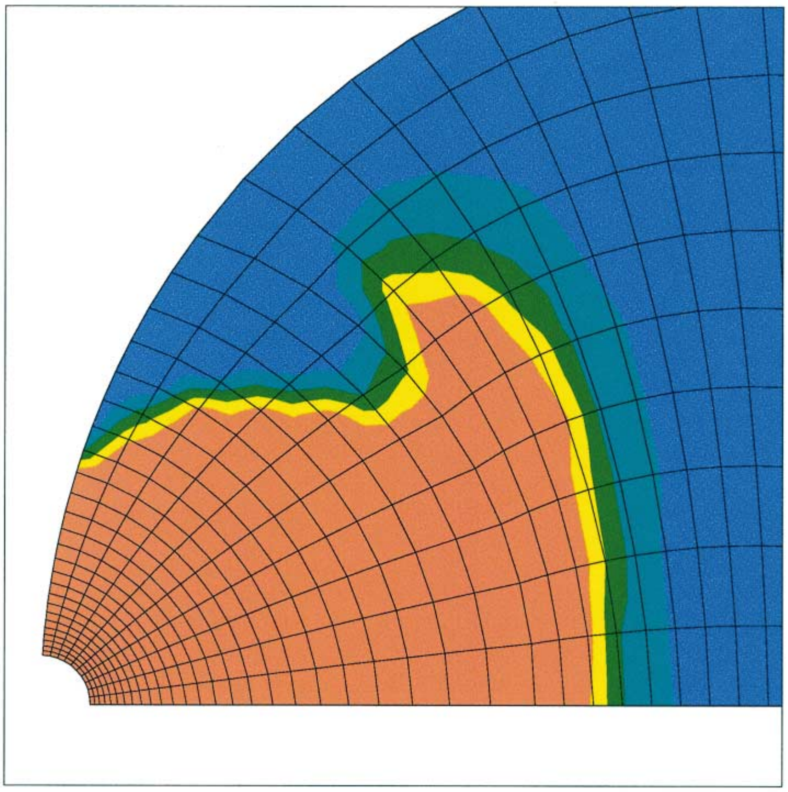

Fig. 9—continued.

(d)

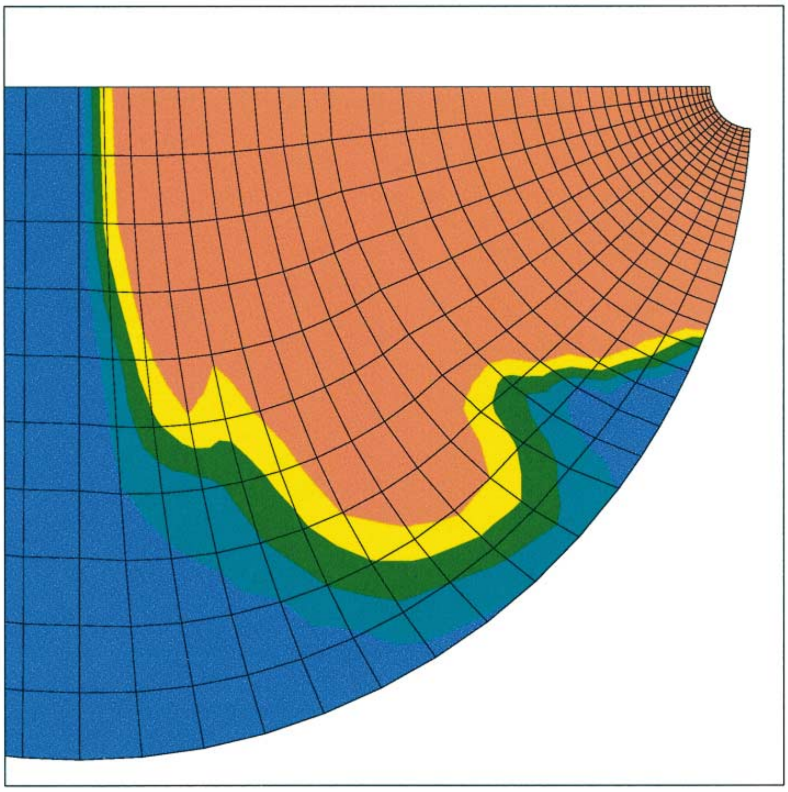

Fig. 9—continued.

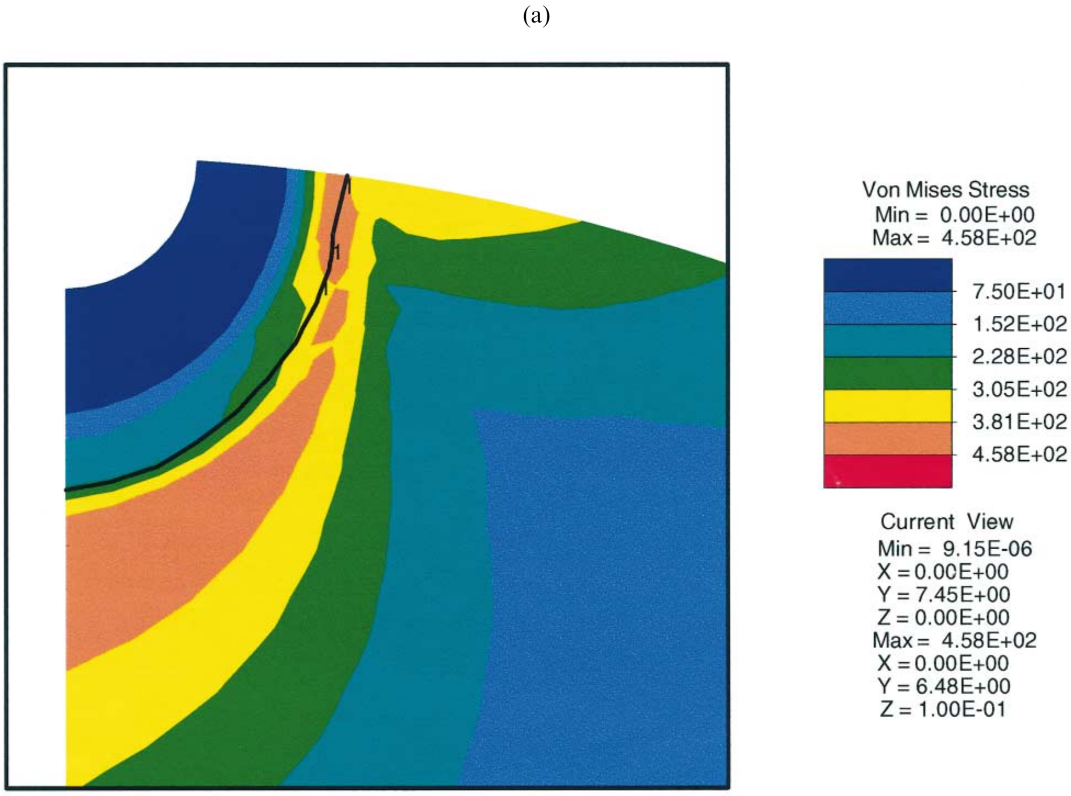

Fig. 11. Level contours of effective Mises stress on the crack plane showing plastic zone size ($\sigma \geqslant \sigma_Y = 311$ MPa). (a) $N = 255{,}000$ cycles; (b) $N = 330{,}000$ cycles; (c) $N = 340{,}000$ cycles, and (d) $N = 345{,}000$ cycles. The level contours $D = 0.8$ are also shown for reference as dark lines.

(b)

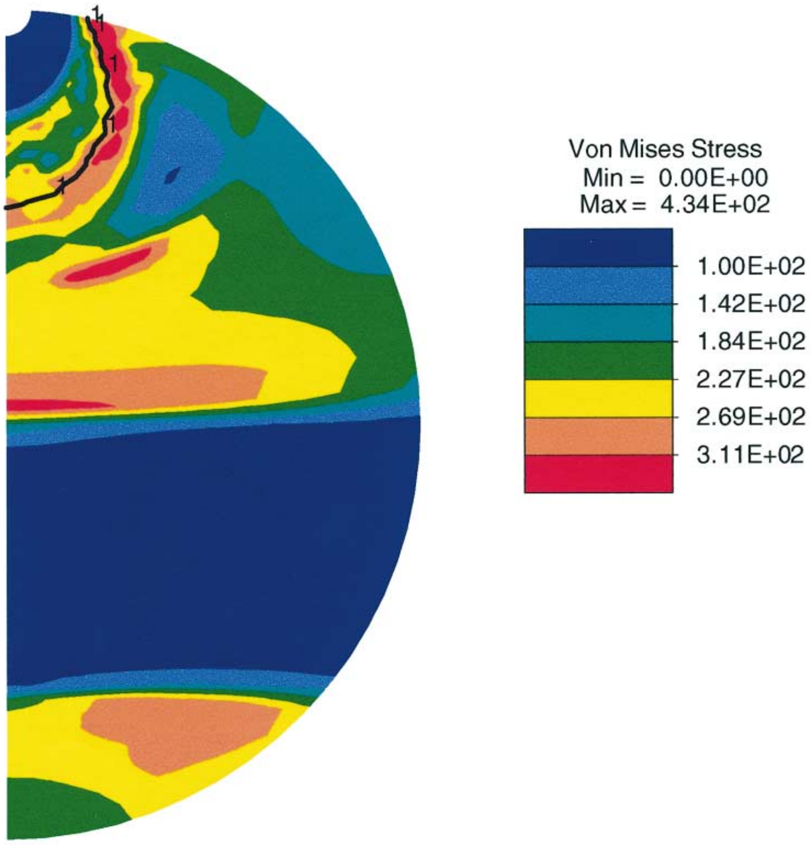

Fig. 11—continued.

(c)

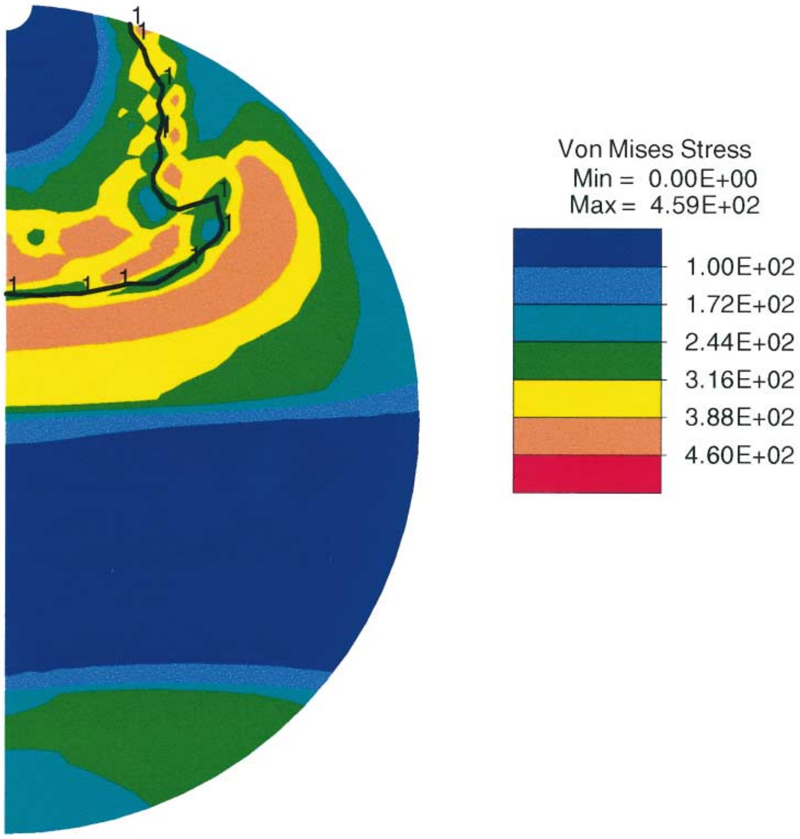

Fig. 11—continued.

(d)

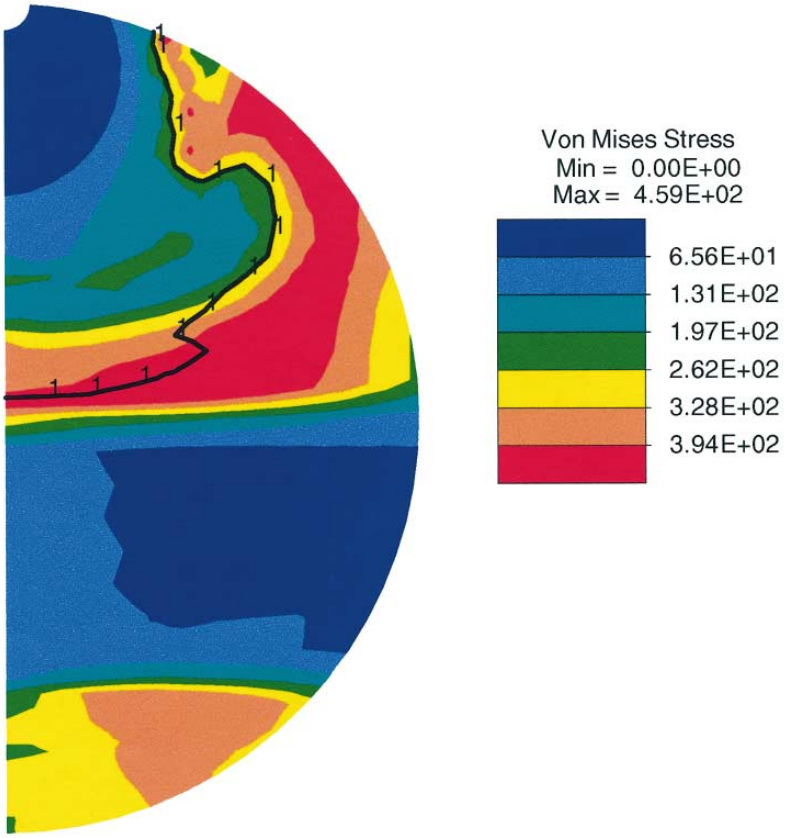

Fig. 11—continued.

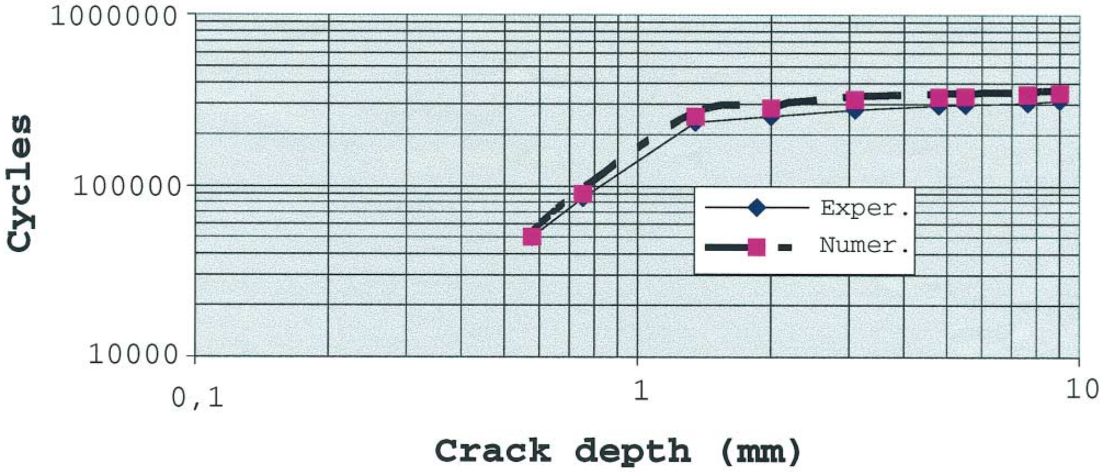

Fig. 12. Experimental (Thompson and Sheppard, 1992a, b, c) vs. predicted fatigue life curves.

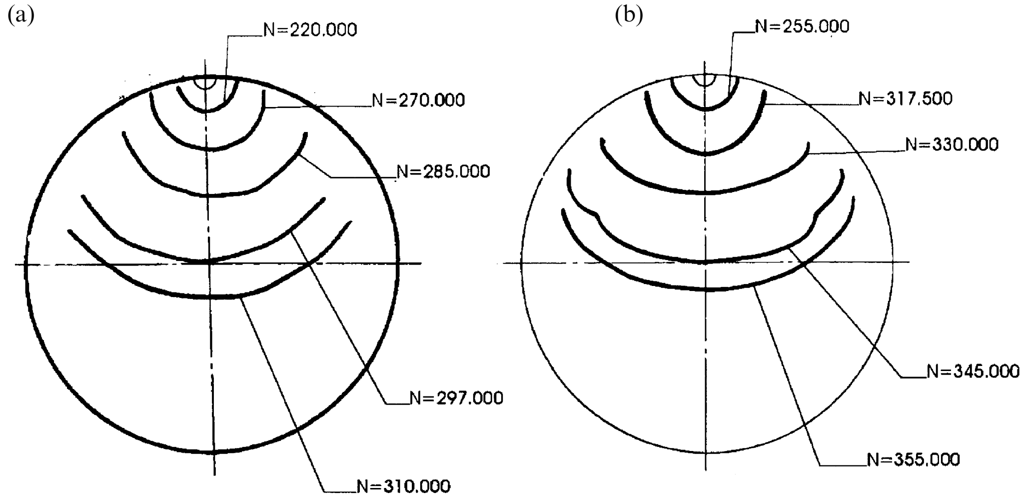

Fig. 10. Progression of beachmark crack fronts with number of cycles. (a) Experimental (Thompson and Sheppard, 1992a, b, c); (b) computed.

crack extends to about two thirds of the cross section of the shaft, the remaining ligament is fully plastic and linear-elastic fracture mechanics is no longer applicable.

It is also illuminating to estimate the width R of the cohesive zone. Using the Dugdale–Barenblatt solution by way of reference gives

$$R = \frac{\pi}{8} \frac{E}{1-\nu^2} \frac{G_c}{\sigma_c^2} = 11\,\mathrm{mm} \tag{37}$$

The convergence studies of Camacho and Ortiz (1996) and de Andrés (1997) reveal that the accuracy of cohesive elements requires that the mesh resolve the cohesive zone, i.e., that the mesh size $h \ll R$ over the cohesive zone. In the case under consideration, the corresponding restriction on the mesh size is that $h \ll 11$ mm, which, evidently, is not a stringent condition.

The computational mesh is shown in Fig. 8. The observational evidence (Thompson and Sheppard, 1992a, b, c) reveals that the crack propagates within its plane throughout the test. By virtue of the symmetry of the problem, the analysis may be restricted to one half of the shaft. The shaft is discretized using the enhanced 3-D elastoplastic brick of Simó et al. (1993) and the plane of the crack is tiled with cohesive elements. The mesh contains a total of 10,304 nodes, 8625 brick elements and 505 cohesive elements, resulting in 28,980 equilibrium equations. The calculations were carried out using R. L. Taylor's finite element program FEAP (Taylor and Simó).

Figure 9 shows the distribution of the damage variable D over the plane of the crack after $N = 255{,}000$, 330,000, 340,000 and 345,000 loading cycles. The level contours of D effectively reveal the geometry of the crack, corresponding to a value of $D \approx 1$; the uncracked ligament, $D \approx 0$; and the cohesive zone, $0 < D < 1$. The computed sequence of crack fronts, conventionally identified with the level contour $D = 0.8$, is shown in Fig. 10, which also collects the observations of Thompson and Sheppard (1992a, b, c) by way of comparison. In addition, Fig. 11 depicts the distribution of the effective Mises stress σ on the crack plane after the same number of cycles. The plastic zone is evident in this figure as the region where $\sigma \geqslant \sigma_Y = 311$ MPa. Finally, the computed number-of-cycles vs crack-length curve is compared to the experimental measurements of Thompson and Sheppard (1992a, b, c) in Fig. 12. Following these authors, the crack length is measured along the surface of the shaft.

Several aspects of these results are noteworthy. In keeping with estimate (36), the computed size of the plastic zones is well beyond the limits of the small-scale yielding assumption central to linear elastic fracture mechanics. This underscores the usefulness of cohesive element formulations in fully-yielded situations. Another interesting feature is the markedly larger size of the plastic zone near the free surface, Fig. 11a. Evidently, this is due to the loss of constraint and the dominance of plane stress conditions near the free surface. Indeed, telltale shear lips characteristic of plane-stress crack-tip plastic zones have been extensively documented by Thompson and Sheppard (1992c).

An immediate effect of the development of shear lips is the retardation of the crack front near the free surface, an effect which is clearly apparent in Fig. 9. The point where the crack front meets the free surface acts as an anchorage point which locally slows down the rate of crack growth. Indeed, the experimentally observed beachmarks bear out this prediction, Fig. 10. We note in passing the close agreement between the computed and experimental beachmarks. It is also interesting to note that, in keeping with the estimate (37), the computed cohesive zones are quite wide and, consequently, the mesh size required to resolve the cohesive zones is tolerably large.

By way of sharp contrast, the portions of the crack front located deep inside the shaft grow comparatively faster. Remarkably, this growth-rate differential eventually causes the internal crack front to tunnel towards the surface, Fig. 9c. By this tunneling mechanism, the crack effectively defeats the stabilizing effect of the shear lips, which results in a sudden increase in the rate of growth of the crack. These different stages of growth are reflected in the fatigue life curve, Fig. 12. In particular, the sharp acceleration in growth rate due to tunneling is clearly apparent at about 300,000 cycles. Here again, the close agreement between the computed and measured fatigue life curve is quite remarkable.

6. Summary and discussion

We have developed a three-dimensional cohesive element and a class of irreversible cohesive laws which enable the accurate and efficient tracking of three-dimensional fatigue crack fronts and the calculation of the attendant fatigue life curves. The cohesive element governs the separation of the crack flanks in accordance with an irreversible cohesive law, eventually leading to the formation of free surfaces, and is compatible with a conventional finite element discretization of the bulk material. The theory permits the incorporation into the analysis of bona fide fracture parameters such as the cohesive strength and the fracture energy. An appealing feature of this approach is that it does not presuppose a particular type of constitutive response of the material, the extent of crack growth, or the size of the plastic zone. The shape and location of successive crack fronts is also an outcome of the calculations.

The versatility and predictive ability of the method is demonstrated through the simulation of the axial fatigue tests on aluminum shafts of Thompson and Sheppard (1992a, b, c). The prediction of three-dimensional fatigue crack growth is, to the best of our knowledge, a novel application of cohesive elements. The specimens in the experiments of Thompson and Sheppard experience fully yielded conditions and thus are outside the scope of linear elastic fracture mechanics and Paris' law. This underscores the general applicability of cohesive elements. The calculations reveal insights—and furnish detailed information—about the formation of shear lips and the attendant slowdown of the crack near the surface; and the way in which the crack defeats the shear lips by tunneling inside the specimen. The ability of the method to reproduce the experimentally observed progression of beachmarks and fatigue life curves is particularly remarkable.

Acknowledgements

The authors are grateful to Iberdrola, S.A. for financial support. M.O. gratefully acknowledges support from the Office of Naval Research through grant N00014-96-1-0068.

References

de Andrés, A., 1997. Fatiga multiaxial en ejes de gran par, (in Spanish) Ph.D. thesis, E. T. S. de Ingenerios Industriales, Universidad Pontificia de Comillas, Madrid (Spain).

Azodi, D., Bachmann, P., 1993. Numerical analysis of cyclic deformation and crackgrowth of precracked steel components using the ADINA program system. Computers and Structures 47, 565–589.

Barrenblatt, G.I., 1962. The mathematical theory of equilibrium of cracks in brittle fracture. Adv. Appl. Mech. 7, 55–129.

Beltz, G.E., Rice, J.R., 1991. Dislocation nucleation vs cleavage decohesion at crack tips. In: Lowe, T.C., Rollett, A.D., Follansbee, P.S., Daehn, G.S. (eds.), Modeling the Deformation of Crystalline Solids: Physical Theory, Application and Experimental Comparisons. TMS: Warrendale, PA, pp. 457–480.

Camacho, G.T., Ortiz, M., 1996. Computational modeling of impact damage in brittle materials. Int. J. Solids Struct. 33, 2899–2938.

Chen, W.N., Ravichandran, G., 1994. Dynamic compressive behavior of ceramics under lateral confinement. J. Phys. IV, 4, 177–182.

Chen, W.N., Ravichandran, G., 1996. Static and dynamic compressive behavior of aluminum nitride under moderate confinement. J. Amer. Ceram. Soc. 79, 579–584.

Dugdale, D.S., 1960. Yielding of steel sheets containing slits. J. Mech. Phys. Solids 8, 100–104.

Forman, R.G., Shivakumar, V., 1986. Growth behavior of surface cracks in the circumferential plane of solid and hollow cylinders. Fracture Mechanics, Vol. 17. ASTM STP 905, pp. 59–74.

Hillerborg, A., Modeer, M., Petersson, P.E., 1976. Analysis of crack formation and crack growth in concrete by means of fracture mechanics and finite elements. Cement Concrete Research 6, 773–782.

Kassir, M.K., Sih, G.C., 1966. Three-dimensional stress distribution around an elliptical crack under arbitrary loadings. Journal of Applied Mechanics 33, 602.

Lubliner, J., 1972. On the thermodynamic foundations of non-linear solids mechanics. International Journal of Non-Linear Mechanics 7, 237–254.

Lubliner, J., 1973. On the structure of the rate equations of materials with internal variables. Acta Mechanica 17, 109–119.

Marsden, J.E., Hughes, T.J.R., 1983. Mathematical Foundations of Elasticity. Prentice-Hall, Englewood Cliffs, N.J.

Marusich, T.D., Ortiz, M., 1995. Modelling and simulation of high-speed machining. International Journal for Numerical Methods in Engineering 38, 3675–3694.

Needleman, A., 1987. A continuum model for void nucleation by inclusion debonding. Journal of Applied Mechanics, ASME, 54, 525–531.

Needleman, A., 1990a. An analysis of tensile decohesion along an imperfect interface. Int. J. Fract. 42, 21–40.

Needleman, A., 1990b. An analysis of tensile decohesion along an interface. J. Mech. Phys. Solids 38, 289–324.

Needleman, A., 1992. Micromechanical modeling of interfacial decohesion. Ultramicroscopy 40, 203–214.

Ortiz, M., 1988. Microcrack coalescence and macroscopic crack growth initiation in brittle solids. Int. J. Solids Structures 5, 213–250.

Ortiz, M., Suresh, S., 1993. Statistical properties of residual stresses and intergranular fracture in ceramic materials. J. of Appl. Mech. 60, 77–84.

Planas, J., Elices, M., Guinea, G.V., 1994. Cohesive cracks as a solution of a class of nonlocal problems. In: Bazant, Z.P. (Ed.), Fracture and Damage in Quasibrittle Structures.

Rice, J.R., 1968. Mathematical analysis in the mechanics of fracture. Liebowitz, H. (Ed.), Fracture, Vol. 2. Academic Press, New York, pp. 191–311.

Rice, J.R., 1992. Dislocation nucleation from a crack tip: an analysis based on the Peierls concept. J. Mech. Phys. Solids 40, 235–271.

Rose, J.H., Ferrante, J., Smith, J.R., 1981. Universal binding energy curves for metals and bimetallic interfaces. Phys. Rev. Letters 47, 675.

Simó, J.C., Armero, F., Taylor, R.L., 1993. Improved versions of assumed enhanced strain tri-linear elements for 3-D finite deformation problems. Comp. Meth. Appl. Mech. Engr. 110, 359–386.

Taylor, R.L., Simó, J.C., Private communication.

Thompson, K.D., Sheppard, S.D., 1992a. Stress-intensity factors in shafts subjected to torsion and axial loading. Eng. Fract. Mech. 42, 1019–1034,

Thompson, K.D., Sheppard, S.D., 1992b. Fatigue crack-growth in notched and plain shafts subjected to torsion and axial loading. Eng. Fract. Mech. 43, 55–71.

Thompson, K.D., Sheppard, S.D., 1992c. Growth of shear lips in surface cracked shafts subjected to fatigue loading. Eng. Fract. Mech. 43, 73–82.

Tvergaard, V., Hutchinson, J.W., 1993. The influence of plasticity on mixed-mode interface toughness. J. Mech. Phys. Solids 41, 1119–1135.

Tvergaard, V., Hutchinson, J.W., 1996a. Effect of strain dependent cohesive zone model on predictions of interface crack growth. J. Phys. IV 6, 165–172.

Tvergaard, V., Hutchinson, J.W., 1996b. Effect of strain dependent cohesive zone model on predictions of crack growth resistance. Int. J. Solids Struct. 33, 3297–3308.

William, K., 1989. Simulation issues of distributed and localized failure computations. In: Mazars, J., Bazant, Z.P. (Eds.), Cracking and Damage. Elsevier Science, New York, pp. 363–378.

Xu, X.P., Needleman, A., 1993. Void nucleation by inclusion debonding in a crystal matrix. Modelling and Simulation in Materials Science and Engineering, 1, 111–132.

Xu, X.-P., Needleman, A., 1994. Numerical simulations of fast crack growth in brittle solids. J. Mech. Phys. Solids, submitted.

Xu, X.P., Needleman, A., 1996a. Numerical simulations of dynamic interfacial crack-growth allowing for crack-growth away from the bond line. Int. J. Frac. 74, 253–275.

Xu, X.P., Needleman, A., Numerical simulations of dynamic crack-growth along an interface. Int. J. Frac. 74, 289–324.